Tectonic stressing in California modeled from GPS observations

Tom Parsons[1]

Received 18 July 2005; revised 24 October 2005; accepted 11 December 2005; published 21 March 2006.

[1] What happens in the crust as a result of geodetically observed secular motions? In this paper we find out by distorting a finite element model of California using GPS-derived displacements. A complex model was constructed using spatially varying crustal thickness, geothermal gradient, topography, and creeping faults. GPS velocity observations were interpolated and extrapolated across the model and boundary condition areas, and the model was loaded according to 5-year displacements. Results map highest differential stressing rates in a 200-km-wide band along the Pacific-North American plate boundary, coinciding with regions of greatest seismic energy release. Away from the plate boundary, GPS-derived crustal strain reduces modeled differential stress in some places, suggesting that some crustal motions are related to topographic collapse. Calculated stressing rates can be resolved onto fault planes: useful for addressing fault interactions and necessary for calculating earthquake advances or delays. As an example, I examine seismic quiescence on the Garlock fault despite a calculated minimum 0.1–0.4 MPa static stress increase from the 1857 $M\sim7.8$ Fort Tejon earthquake. Results from finite element modeling show very low to negative secular Coulomb stress growth on the Garlock fault, suggesting that the stress state may have been too low for large earthquake triggering. Thus the Garlock fault may only be stressed by San Andreas fault slip, a loading pattern that could explain its erratic rupture history.

Citation: Parsons, T. (2006), Tectonic stressing in California modeled from GPS observations, *J. Geophys. Res.*, *111*, B03407, doi:10.1029/2005JB003946.

1. Introduction

[2] Earthquakes result from elastic stress built up in part by tectonic motion. GPS-derived crustal strain measurements provide an opportunity to model the relative growth of crustal stress in detail. The observed strain field is not uniform, thus it is expected that the distribution of crustal stress will also be irregular. Crustal volumes with high stressing rates that are not associated with high seismicity rates could be future earthquake locations. Additionally, estimated stressing rates on particular faults enable calculations of advances or delays from stress interactions. In this paper, the stressing rate in California is calculated with a three-dimensional (3-D) finite element model that is loaded by topography and the observed GPS strain field.

[3] A complex model of the California lithosphere was required because of highly variable structure; the model must incorporate thin Pacific oceanic crust in the west and the thickened batholithic Sierra Nevada block to the east. Associated topographic differences among crustal provinces may also influence the stress state. In addition, observed heat flow is highly variable across the state and, by inference, the viscoelastic properties at depth are also expected to vary. A statewide model must also account for major fault zones that creep continuously in some sections and that are locked in others. Finally, to benefit from the details of the spatially variable GPS-derived loading, the model must be a continuum solution rather than one composed of rigid blocks.

[4] The GPS-derived strain field contains components of many simultaneous processes: deformation caused by plate motions, topographic collapse, volcanic inflation, coseismic slip during earthquakes, and postseismic effects such as viscoelastic relaxation, and poroelastic changes [e.g., *Segall and Davis*, 1997]. Thus loading a model with GPS-derived strains inherently incorporates diverse stressing processes without the complications of modeling them individually. A potential drawback is that a fundamental assumption must be made. GPS measurements are recorded at the Earth's surface and might reasonably be expected to represent strain in the elastic part of the lithosphere that is coupled to the surface. Thus a model loaded according to surface strain assumes that the substrate beneath the elastic lithosphere is passive, and does not drive the system. This may be a valid assumption in strike-slip California [e.g., *Parsons*, 2002], but is expected to break down in subduction systems where the driving process is deep, and often partially decoupled from the surface. Here I assume that deformation at the surface represents motion of the elastic core of the lithosphere, and that deformation tapers with depth into the increasingly inviscid substrate.

2. Model Features and Strategy

[5] The model was developed primarily to study stressing in the seismogenic crust of strike-slip California. However,

[1]U.S. Geological Survey, Menlo Park, California, USA.

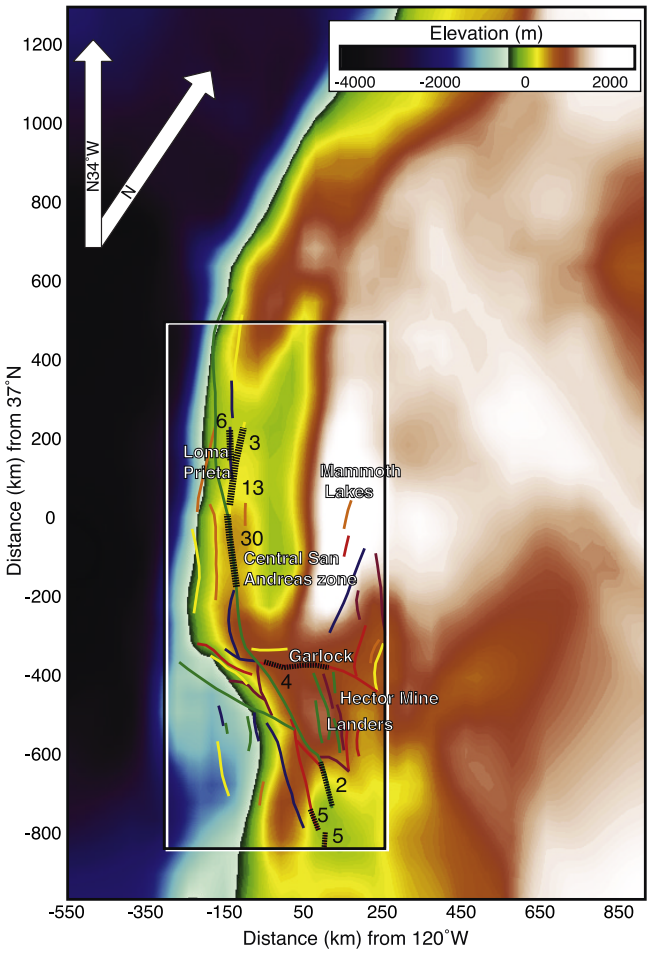

Figure 1. Region modeled in this study. The box outlines the primary volume of interest, and some major fault zones are shown. The surrounding areas are included in the model to ensure proper boundary conditions. The model edges are parallel and perpendicular to N34°W to be more aligned with the coastline. Colors are contours of smoothed topography/bathymetry used in the model. Black dashed faults are creeping segments in the model, and the associated numbers are mean creep rates in mm yr^{-1} [*Thatcher*, 1990].

that region is influenced by tectonism on all sides that must be accounted for along the model boundaries (Figure 1). To the west, the Pacific plate moves past at about 34–39 mm yr^{-1} on a N30°–35°W vector [*DeMets et al.*, 1994; *Argus and Gordon*, 2001; *Savage et al.*, 2004; *d'Alessio et al.*, 2005] relative to the Sierra Nevada block (treated as the reference frame for this study). The Basin and Rage province impinges from the east via spatially varying rates of extension and shearing [e.g., *Hammond and Thatcher*, 2004]. To the north, the Cascadia subduction zone converges with the Sierra Nevada block at about 11 mm yr^{-1} [e.g., *Wells et al.*, 1998]. On the southern edge of the model, the San Andreas strike-slip system evolves into the oceanic spreading center of the Gulf of California [e.g., *Lonsdale*, 1989]. These regions make up the boundaries of the model and their observed deformation is part of the input loads.

[6] In this study, the focus is on active faults in strike-slip California (boxed area in Figures 1–12). The boundary condition regions of the model extend well past the study area so that reasonable estimates of their effects are modeled. However, boundary condition regions have not been modeled with the same level of detailed crustal structure and heat flow variability as the study area because localized variation in tectonic stressing inside the boundary regions was not of primary interest.

2.1. Topography and Lithosphere Structure

[7] A challenging aspect to modeling a large region like California and surroundings is the extreme variation in crustal structure that transitions from thin, warm oceanic lithosphere into the thick, cold Sierra Nevada block across a few hundred km. Large changes in elastic thickness and topography can affect how stress is transmitted. A smoothed topographic/bathymetric surface (Figures 1 and 4) defines the top of the model, which is built in three layers. The base of the upper crustal layer is defined by seismic

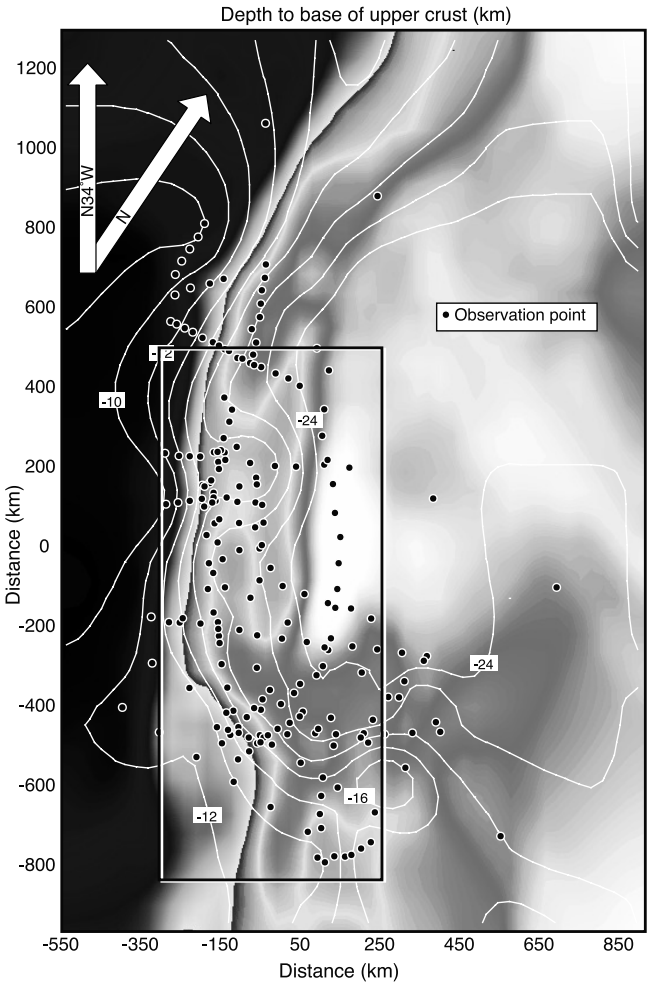

Figure 2. Contours of depth below sea level to the base of the upper (silicic) crust as determined from seismic studies (references given in the text). The black dots show sample locations and are the basis for contouring. These contours define the base of the top layer in the finite element model. The box shows the study area.

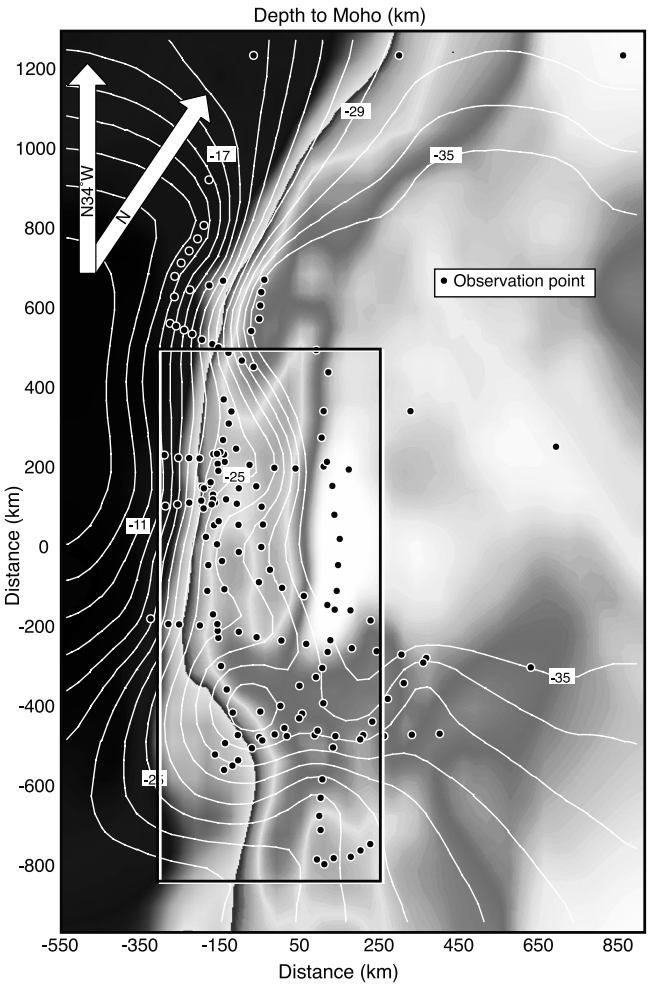

Figure 3. Contours of depth below sea level to the base of the crust as determined from seismic studies (references given in the text). The black dots show sample locations and are the basis for contouring. These contours define the base of the middle layer (lower crust) and the top of the bottom layer (upper mantle) in the finite element model. The box shows the study area.

measurements that report a change in seismic velocity associated with silicic rocks into more mafic lower crust (V_p > 6.5 km s^{-1}) (Figure 2), and a second layer is defined to lie between the upper crust and the Moho (V_p > 7.9 km s^{-1}) (Figure 3) [*Prodehl*, 1979; *Walter and Mooney*, 1982; *Colburn and Mooney*, 1986; *Holbrook and Mooney*, 1987; *Howie et al.*, 1993; *Page and Brocher*, 1993; *Catchings and Kohler*, 1996; *Fliedner and Ruppert*, 1996; *Holbrook et al.*, 1996; *Parsons and McCarthy*, 1996; *Godfrey et al.*, 1997; *Hauksson and Haase*, 1997; *Henstock et al.*, 1997; *Beaudoin et al.*, 1998; *Leitner et al.*, 1998; *Hauksson*, 2000; *ten Brink et al.*, 2000; *Fuis et al.*, 2001]. The third layer represents the upper mantle and persists to a depth of 100 km, which encompasses the ~5- to 55-km thickness of the mantle lithosphere [e.g., *Melbourne and Helmberger*, 2001]. The model edges are parallel and orthogonal to N34°W (roughly the Pacific-Sierra Nevada relative motion vector), and all model coordinates are in km in a Mercator projection.

[8] Crustal structure in the model was defined by seismic velocity transitions that are assumed here to result from compositional change. Thus physical properties of the upper crustal layer were approximated by wet Westerly granite (Table 1). The lower crustal layer had properties representative of basalt-diabase composition. The upper mantle layer had properties associated with an average of wet and dry dunite samples.

2.2. Finite Element Mesh and Modeling Method

[9] The three model layers have irregular boundaries and were thus meshed with tetrahedral elements (Figure 4). Meshing was conducted using higher-order 3-D elements with quadratic displacement behavior that is best suited to modeling irregular meshes. Elements were defined by 10 nodes, each having 3 degrees of freedom (translations in the nodal x, y, and z directions). All elements in this study had capability of elastic and inelastic deformation, with inelastic strain behavior defined by a rate-dependent creep relation (discussed in section 2.3).

[10] Volumes were meshed by first estimating element edge lengths for all defining lines. The element edge lengths on these lines were then refined for curvature and proximity of features in the geometry. The mesh was thus finest where volumes change shapes the most, and in regions of greatest complexity such as fault terminations or intersections. Since the mesh was scaled by line lengths, elements in the thinnest parts of the crustal layers were much smaller than in the thickest parts (Figure 4). A variable-sized mesh approach reduced the number of nodes in parts of the volumes where they were not needed, making the model more computationally efficient without sacrificing accuracy. The model was composed of 136447 elements defined by 212016 nodes.

[11] To account for stressing resulting from aseismic fault creep, the finite element model had cuts in it that represented major creeping faults in California (Figure 1) [*Thatcher*, 1990]. The faults were deformable, and were constructed from contact elements obeying the Coulomb failure relation

$$CF \equiv \bar{\tau}_f + \mu(\sigma_n), \tag{1}$$

where $\bar{\tau}_f$ is shear stress acting on a fault surface, μ is the friction coefficient, and σ_n is the component of stress acting normal to a fault surface. Contact elements had zero thickness and were welded to the sides of tetrahedral elements.

[12] All modeling presented here was conducted using the ANSYS® finite element program. ANSYS employs the Newton-Raphson approach to solve nonlinear problems. In this method, a load was subdivided into a series of increments applied over several steps. Before each solution, the Newton-Raphson method evaluated the out-of-balance load vector, which is the difference between the restoring forces (the loads corresponding to the element stresses) and the applied loads. A linear solution was performed using the out-of-balance loads. If convergence criteria were not satisfied, then the out-of-balance load vector was reevaluated, the stiffness matrix updated, and a new solution was obtained. The system of equations was solved through direct elimination of

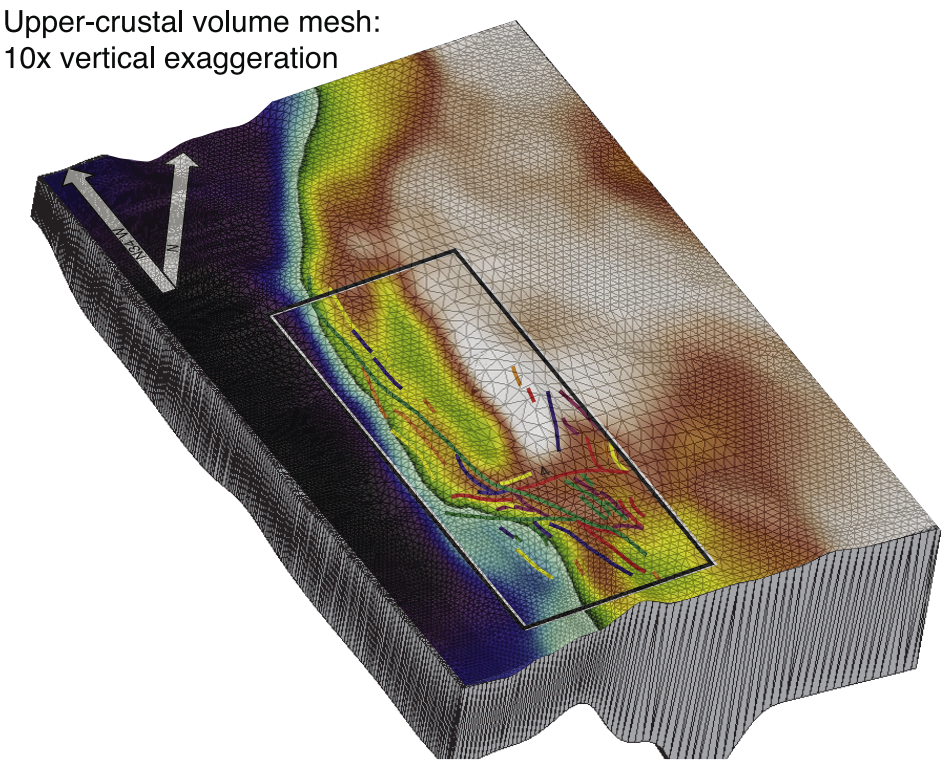

Figure 4. Example of the meshed upper crustal volume shown with 10X vertical exaggeration so that topographic relief is evident. Black lines show boundaries of variable tetrahedral mesh, which is finer in areas of greatest detail. The average element size is roughly 5 × 5 km. Shaded relief contouring, fault lines, and the study area box are draped onto the model for location purposes.

equations until the problem converges (sparse direct solver).

2.3. Heat Flow/Power Law Rheology

[13] To model crustal stress accumulation, it's necessary to simulate the transition from elastic, seismic deformation into viscoelastic, aseismic deformation. This transition is depth-dependent, with deeper, hotter rocks less able to store elastic strain energy over time because they deform anelastically in response to imposed stress at rates that depend on temperature. In the California finite element model, the proportion of inelastic to elastic behavior of a given element node is governed by a crustal geotherm derived from heat flow measurements (Figure 5). I applied the relation [*Meissner*, 1986]

$$T(z) = T_0 + \left(\frac{q^*}{K}\right)z + \left(\frac{A_0 H^2}{K}\right)\left[1 - \exp\left(\frac{-z}{H}\right)\right], \qquad (2)$$

where T is temperature (T_0 is surface temperature), z is depth, K is thermal conductivity, A_0 is heat production defined from an assumption of exponentially decreasing heat production as $A(z) = A_0 \exp(-z/H)$ [*Lachenbruch*, 1968], where H is the relaxation depth such that $A = A_0/e$ ($z = H$), defined here as the base of the upper crust, and $q^* = q_0 + AH$, where q_0 is surface heat flow. The observed heat flow values shown in Figure 5 were interpolated/extrapolated to a 25-km-spaced grid, and separate temperature-depth relations were calculated for each surface point. Temperatures were interpolated between defined geotherms at each model node throughout the 3-D volume to define inelastic behavior. Once defined and assigned, model node temperatures were held constant throughout the calculations.

[14] Postseismic and other transient geodetic observations are well matched with models using power law descriptions of lithospheric rheology [e.g., *Freed and Bürgmann*, 2004], where strain rate depends on differential stress raised to a power. All elements of the California finite element model strained through a combination of linear elasticity and rate-dependent creep behavior. Time-independent elastic strain (ε) occurred in the model according to

$$\varepsilon = \frac{\sigma}{E}, \qquad (3)$$

where E is Young's modulus and σ is differential stress. Modeled time-dependent inelastic strain rate ($\dot{\varepsilon}$) was controlled by the creep equation [e.g., *Kirby and Kronenberg*, 1987]

$$\dot{\varepsilon} = A \exp(-Q_c/RT)\sigma^n, \qquad (4)$$

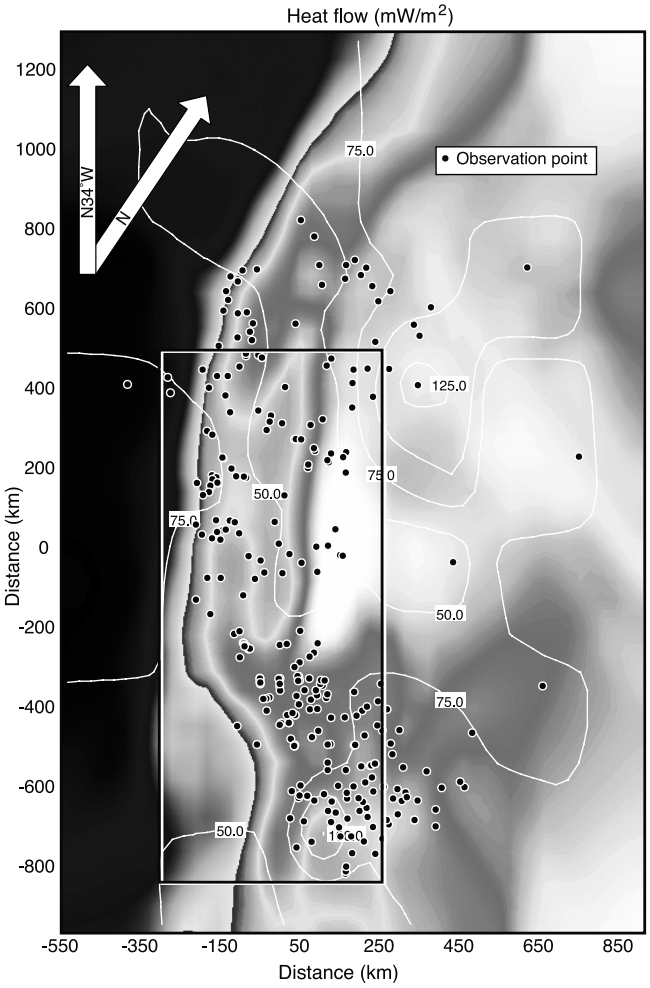

Figure 5. Contours of surface heat flow in mW m^{-2}. The black dots show measurement locations. Model rheology is governed by a geotherm extrapolated from surface heat flow. The box shows the study area.

where A, Q_c (activation energy), and n are experimentally derived constants, R is the universal gas constant, and T is temperature (Table 1). Equation (4) added an increasingly important contribution to modeled strain with increasing temperature, and simulated a smooth transition from elastic to ductile strain with depth. At low temperatures the exponential term of equation (4) approached unity, causing the creep term to become vanishingly small. With increasing temperature, the contribution of the exponential term became more important. There was thus a gradational change from elastic to ductile deformation that was far less abrupt than if uniform layer viscosities were assigned or if elastic elements were layered above viscoelastic elements. The varying constants associated with the upper crustal, lower crustal, and upper mantle model layers can cause small rheological discontinuities at the layer boundaries, though these were small when compared with thermal effects [e.g., *Parsons*, 2002].

2.4. Model Loading and the GPS Velocity Field

[15] Substantial GPS velocity coverage (including permanent and campaign data) of California and surroundings is processed and archived by the U.S. Geological Survey. After editing for outliers, short-term observations, and other poorly converged velocity values, a total of 770 observations were used (Figure 6). Several steps were taken to utilize the GPS observations in loading the finite element model. First, the velocities needed to be referenced. The reference frame for modeling in this study was the Sierra Nevada block because it shows little internal deformation as compared with the surrounding provinces. Sierra Nevada block velocity was taken as the mean of four stations described by *Dixon et al.* [2000] (CMBB, QUIN, SUTB, UCD1) at -5.8 mm yr^{-1} north and 19.5 mm yr^{-1} east. All horizontal GPS observations were then differenced from these values. The positions of the velocity observations were projected to km and velocity vectors were rotated into a N34°W model coordinate system (Figure 6). Last, a grid of 25-km-spaced points was established, and horizontal velocities were interpolated and extrapolated to the grid

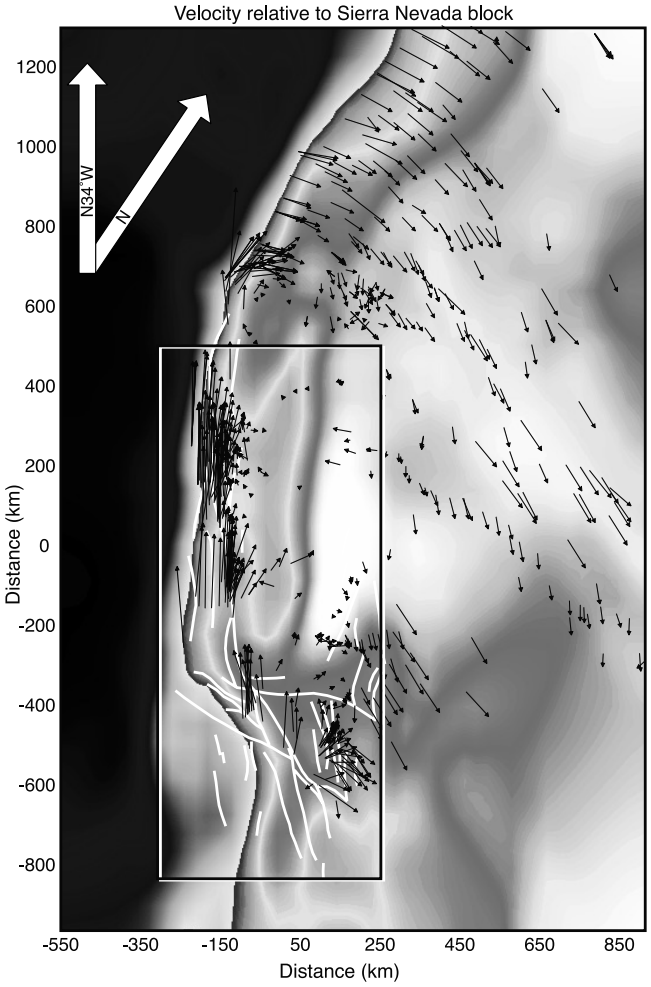

Figure 6. Campaign and permanent GPS observations used to drive model deformation. Data were gathered through U.S. Geological Survey automatic processing and were edited for quality and consistency. Vectors were rotated into the N34°W coordinate system of the model and differenced from observations within the Sierra Nevada block, which is used as the stable reference frame in this study. The box shows the study area.

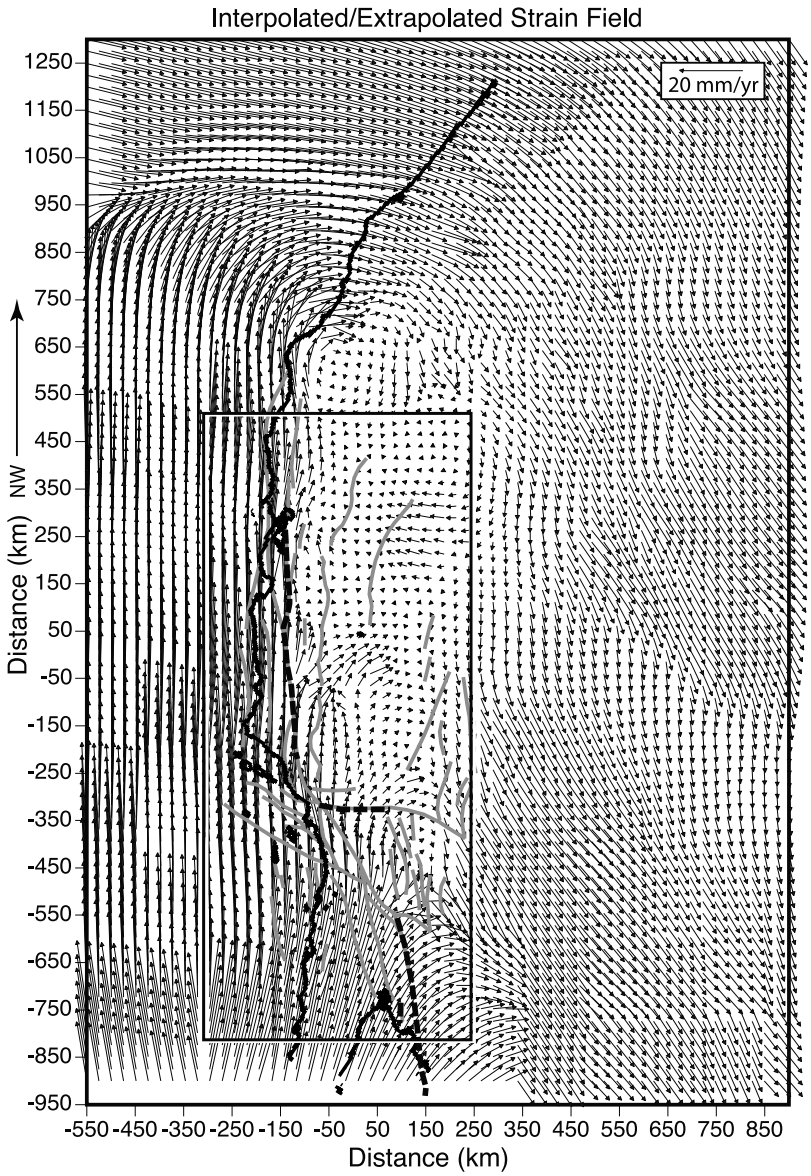

Figure 7. Extrapolated and interpolated velocity field (25-km spacing) from observations shown in Figure 6. The left edges were assigned relative Pacific plate–Sierra Nevada rates south of the Mendocino triple junction, and relative Gorda plate–Sierra Nevada rates to the north. Nearest model nodes were displaced according to this grid. The box shows the study area.

(Figure 7) using a 2-D kriging algorithm. South of the Mendocino triple junction, the left edge of the model was assumed to be moving roughly at Pacific plate velocity (39 mm yr^{-1} N34°W) in the absence of observed values to avoid spurious extrapolations. North of the triple junction the left model edge was assumed to move with the Gorda plate. All upper crustal nodes in the model were then associated with velocities interpolated from the grid (shown in Figure 7) for displacement loads.

2.5. Model Implementation

[16] In the previous sections all the necessary model definitions were described for simulating stress growth in California. The first step in running the model was to subject it to gravity, which compressed the model and established an initial stress state. The bottom of the model was constrained to zero displacement in the vertical direction, and the model sides were not permitted to move laterally. All other nodes were given 3 degrees of freedom. The basal layer in the model was set below the measured extent of the mantle lithosphere (~5- to 55-km thick [*Melbourne and Helmberger*, 2001]). Elements at the model base mimic low-viscosity asthenosphere because of high temperatures. Thus, while compressed because of the fixed basal boundary condition (~3% strain), elements at or near the model base could not support shear stresses or refer any stresses into the upper part of the model (Figure 8).

[17] The model elements had nonlinear time dependence; thus the rate of gravity implementation was important. If the model was subjected to gravity too rapidly, then deforma-

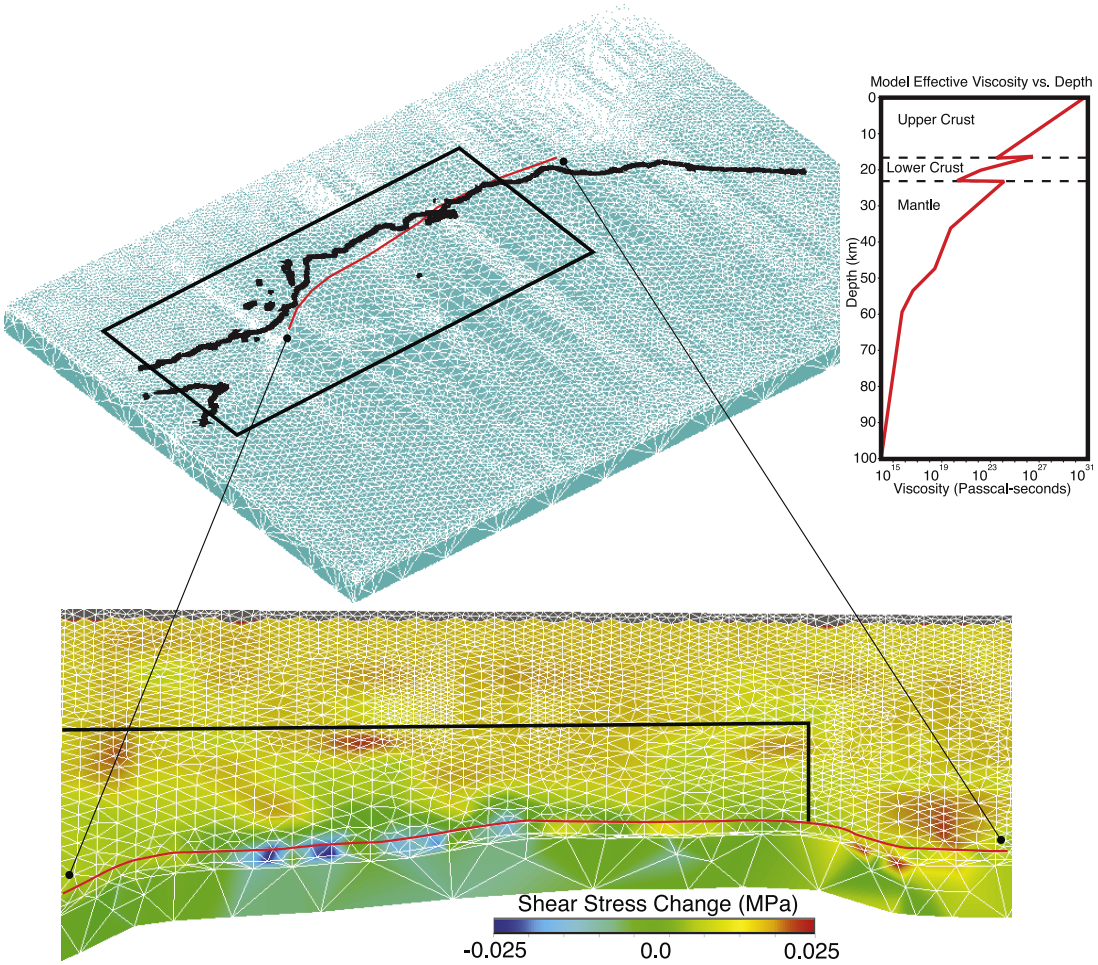

Figure 8. Whole finite element model shown with the study area box and coastline for location. Cut-away below shows accumulated shear stress versus depth along a portion of the San Andreas fault after 5 years of GPS-derived displacements were applied. Very little shear stress develops along the model base because of the low viscosity at depth. An example viscosity profile derived near the San Andreas fault is shown in the inset. Effective viscosity was calculated according to $n = \sigma^{1-n} \exp(Q_c/RT)/2A$, where σ is differential stress (calculated with the finite element model), R is the gas constant, and Q_c (activation energy), A, and n are experimentally determined constants (Table 1). Most of the strength in the model was carried in the crust because a partially wet upper mantle rheology was used.

tion rates higher than could be supported by the defined material time dependence ensued. In this study, gravitational loading was ramped over 25 kyr, and then an additional settling period of 5 kyr was applied to ensure that the model was fully compressed. Time steps were initially 1 year, and gradually increased by a factor of 1.5 per iteration such that the ramping involved 42 time steps. Next, displacements from the GPS grid of Figure 7 were imposed over a 5-year period. In fact, 20 sequential 5-year periods were run to ensure that the stressing rate results were linear in time, and not influenced by the initial stress state. Each 5-year run was initially ramped at 0.1-year time steps to avoid sudden transient deformation induced by displacement loading.

[18] The model was prestressed with gravity prior to loading by GPS. However, the model was not prestressed by relative plate motions because it is impossible to know with sufficient detail all past fault displacements. Thus stress accumulation not relieved by past earthquakes resulting from relative plate motions are not accounted for in the model. This issue is expected to influence modeled stressing rate results presented here only where the past crustal strain tensor components were oriented differently than currently indicated by the GPS deformation field. An example might be a case where current deformation occurs in response to an unrelieved stress concentration. Thus a model of that deformation would calculate an increase in stress, when in fact the observed deformation would be reducing stress.

2.6. Effects of Model Assumptions and Data Limitations

[19] Results presented here depend on the quality of the input data and many assumptions inherent in projecting

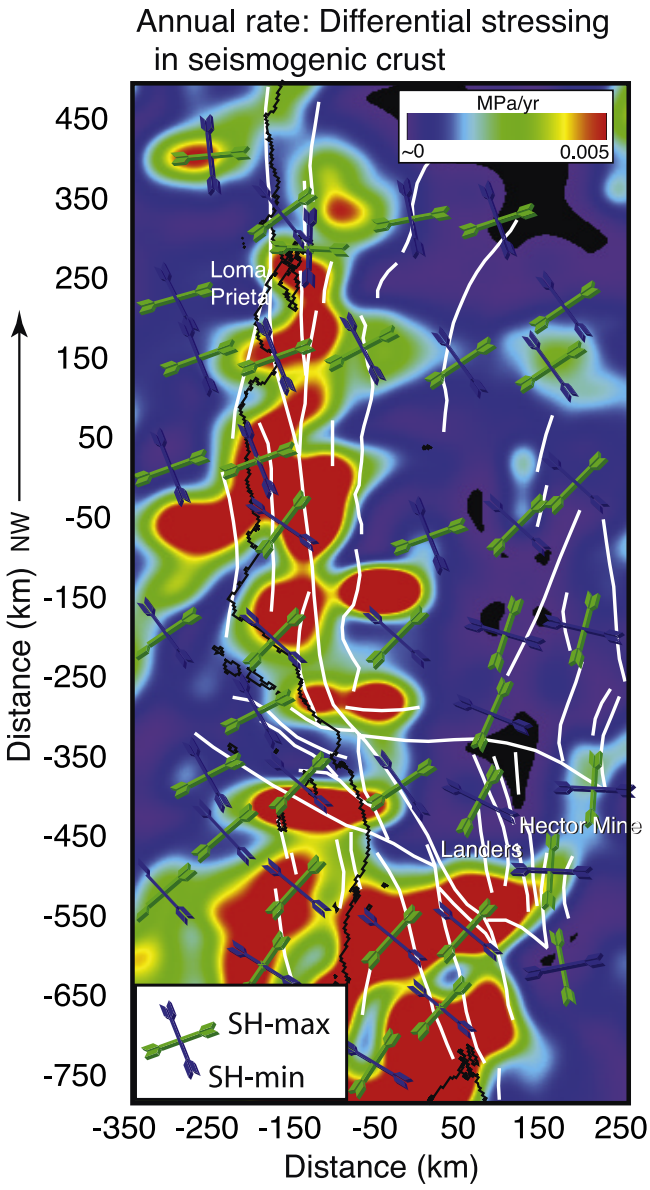

Figure 9. Modeled pattern of differential stressing rate ($\sigma_3 - \sigma_1$) in the seismogenic upper crust of California (depth-averaged) from GPS-derived displacements shown in Figure 7. Warm colors show highest stressing rates, while areas in black show areas of stress reduction, or zero growth. The green and blue arrows show the orientations of maximum and minimum horizontal stress, respectively. White lines show major fault traces for reference.

information measured at the surface to great depth. Surface traces of creeping faults were projected through the crust in this study, when in fact they could be more connected beneath the surface. In most cases, creeping fault segments in the model were isolated (Figure 1) such that connectivity was not an issue; the exception could be the Hayward-Calaveras fault junction in the southern San Francisco Bay region, which has a complex structure [e.g., *Manaker et al.*, 2005] that was impossible to capture at the scale of a statewide model. If creep is more continuous through the junction than the interrupted faults in the finite element model, then stressing rates on the Hayward fault could have been overestimated. In addition, the distribution of creeping and locked fault patches patched is likely more complex [e.g., *Schmidt et al.*, 2005] than could be addressed in the California finite element model.

[20] Gaps of varying distances (Figures 2, 3, 5, and 6) lie between observations of crustal structure, heat flow and GPS displacements. Therefore the model was likely more smoothly varying among these properties than is the real lithosphere. Calculated results should then be considered in that context; if they exist, localized, sharp spatial changes in tectonic stressing rates were not captured by the California finite element model. In addition, if the surface heat flow values used in the calculations are transient and not reflective of longer term lithospheric conditions, then rheological behavior may have been incorrectly projected. Finally, it should be noted that the projection of temperature with depth involved a number of assumptions, as discussed in section 2.3, that fundamentally affected the model rheology. In summary, an attempt was made to include as much detailed information on crustal structure, rheology, and deformation rates as possible, but calculated stressing rate results should be interpreted with the caveat of considerable uncertainty.

3. Results

[21] The finite element method defined a time series of the full stress and strain tensors at all model nodes. In studying volumes of crust I find it useful to examine the differential stressing rate (Figure 9), which is the time derivative of the difference between the magnitudes of the greatest and least principal stresses ($\sigma_3 - \sigma_1$). Under *Anderson*'s [1951] theory, faulting is expected when the difference between the greatest and least principal stresses exceeds shear strength. Fault orientation is expected at an acute angle to the greatest principal stress direction, and depends on friction. Thus a map of differential stress distribution is valid for all fault orientations, unlike a Coulomb stress map, which is valid only for assumed fault orientations and rakes.

[22] Because of the way the California finite element model was loaded, the greatest modeled stressing rates were expected at discontinuities or changes in observed GPS velocity. Over time, discontinuous displacements developed in the model that caused differential stressing. A mapping of depth-averaged differential stress (Figure 9) demonstrates this, with the highest stressing rates occurring broadly across the San Andreas plate boundary zone. Peak differential stressing rates ($\geq$0.005 MPa yr^{-1}) were calculated to occur in a ~200-km-wide band along the San Andreas fault zone. This band is considerably wider, and an order of magnitude lower in amplitude than was obtained by models that calculated stressing rates via loading from deep, slipping dislocations located beneath the major faults [e.g., *Smith and Sandwell*, 2003]. Unfortunately, the pattern of surface deformation can be reproduced either with deep dislocation slip or with distributed loading [e.g., *Lisowski et al.*, 1991; *Savage et al.*, 1999], meaning that the actual driving mechanism remains unknown. Resulting modeled crustal stress distributions are very different depending on

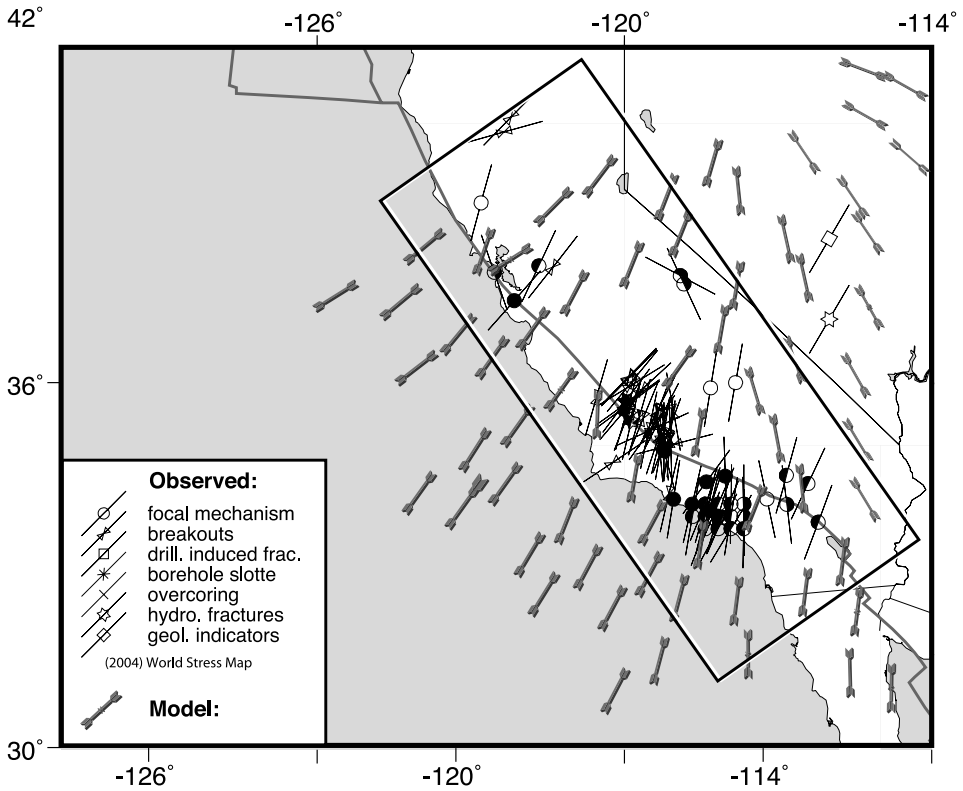

Figure 10. Comparison of modeled orientations of maximum horizontal stress with observations from the World Stress Map project. Modeled directions agree with observed within 10°–20° along the San Andreas fault but differ more significantly outside the study area box in the Basin and Range province.

how tectonic loading is applied [e.g., *Parsons*, 2002], an issue that remains unresolved.

[23] Calculated loading along most of the San Andreas zone is high relative to the rest of map (Figure 9) with the exception of a segment in southern California (∼−300 to −500 km in northwest coordinate). This segment, located just south of the Garlock fault, is associated with fairly uniform GPS velocity on both sides of the fault (Figures 6 and 7) and thus accumulates lower levels of tectonic stress in the model. The 1992 $M = 7.3$ Landers and 1999 $M = 7.1$ Hector Mine earthquakes occurred to the east of this San Andreas fault segment, and the region containing the ruptures is also calculated to have a relatively lower stressing rate. These results suggest that the GPS signal measured coseismic and postseismic deformation. In fact, the mapping of differential stressing rate matches calculations of the post-Landers static stress change [*Stein et al.*, 1992]. A similar, but much smaller effect can be seen near the Loma Prieta earthquake (Figure 9), although comparable variations occur in other places along the San Andreas zone where there have not been $M = 6.9$ events.

[24] Mapping of differential stress rate from GPS shows regions of zero, and even negative stressing rates (plotted in black on Figure 9). In terms of the finite element model, I interpret these regions as deforming in response to the topographic load. The model was preloaded under gravity before the GPS deformation was imposed. Thus areas of calculated stress reduction indicate places where GPS displacements are consistent in direction with deformation caused by gravitational collapse rather than from tectonic plate motions.

[25] Calculated orientations of the minimum and maximum horizontal stresses are plotted on Figure 9. In the model, the orientation of maximum horizontal stress is nearly orthogonal to the San Andreas fault along most of its length, commensurate with observations (Figure 10). However, the model does not match stress orientations in the boundary condition region east of the Sierra Nevada. Conclusions are thus best drawn from the regions along the San Andreas system west of the Sierra block, within the study area box.

3.1. Mapping Stress Rate Versus Radiated Seismic Energy

[26] A fundamental goal of this study was to relate stressing rate with the occurrence of earthquakes. If earthquakes result from stress exceeding frictional resistance along faults as in Coulomb failure (equation (1)), then more earthquakes should be expected where the highest rates of differential stress were mapped. This comparison is somewhat difficult to make because, as was postulated for the southern San Andreas fault, the GPS velocity field includes the coseismic and postseismic effects of earthquakes that affect calculation of the current stressing rate. However,

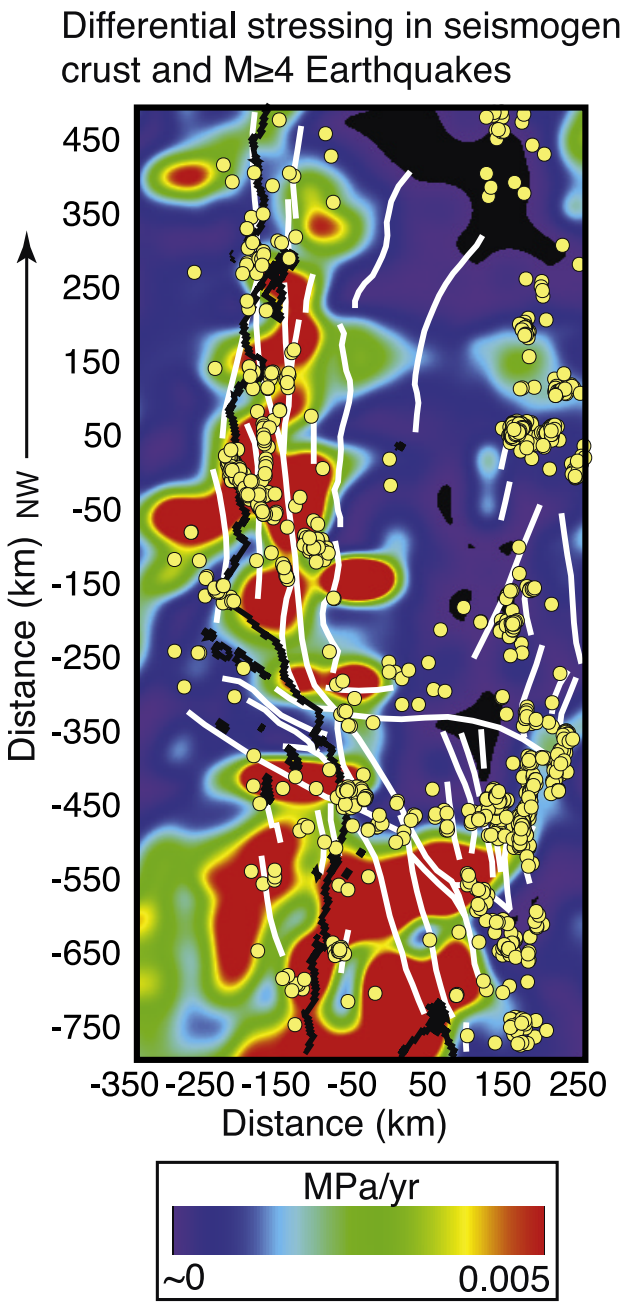

Figure 11. Calculated differential stressing rate shown with $M \geq 4$ earthquake epicenters (1980–2005). Most, but not all, regions with high modeled stressing rates are associated with relatively higher seismicity.

most earthquakes in California have been smaller than the $M = 7.3$ Landers and $M = 7.1$ Hector Mine events over the duration of GPS monitoring and are not expected to have caused as significant a perturbation in the geodetic signal. In Figure 11, $M \geq 4$ earthquake epicenters (1980–2005) are plotted on the differential stressing rate map. Most areas of high stressing rate are associated with the occurrence of earthquakes. Seismicity is low to absent in regions of low or negative stressing rate.

[27] Another way to compare observed seismicity rates to modeled stressing rates is to calculate the radiated seismic energy. *Gutenberg and Richter* [1942, 1956] gave relations between radiated seismic energy E_s and magnitude as

$$\log E_s = 2.4M_b - 1.3 \tag{5}$$

$$\log E_s = 1.5M_s + 4.2, \tag{6}$$

where M_b and M_s are body wave and surface wave magnitudes. The California earthquake catalog has a mixture of several magnitude determinations. However, for the purposes of mapping relative energy release, I used equation (6) for all events and neglected the differences (vanishingly small as discussed later). A map of radiated seismic energy is plotted with the differential stressing rate map in Figure 12 to enable a qualitative comparison between modeled stress input and seismic output.

[28] Examination of stressing rate versus seismic energy release shows areas of correspondence and difference (Figure 12). Seismic energy and stressing are both calculated to occur at relatively high rates along the central San Andreas fault; however, in the eastern San Francisco Bay area the stressing rate is calculated to be relatively higher, while the seismic energy rate is lower (area "1" outlined on Figure 12). An apparent mismatch could indicate a growing seismic gap along the Hayward-Rodgers Creek fault system, which was assigned the highest probability of a M $\geq$ 6.7 earthquake by *Working Group on California Earthquake Probabilities* (*WGCEP*) [2003]. As will be discussed in section 3.1, it isn't possible to quantify the modeled energy imbalance between seismicity and stressing rate without making an assumption about seismic efficiency, the proportion of seismic energy lost through heat generation, fracturing etc.

[29] A second apparent mismatch between seismicity and stressing rate is mapped near the White Wolf fault (area "2" of Figure 12) where the 1952 $M = 7.5$ Kern County earthquake occurred. It may be that postseismic deformation is still part of the GPS signal in this area, manifesting as increased stressing rate in the model. Two additional areas of relatively lower seismic energy release compared with stressing rate are outlined on Figure 12 (areas "3" and "4"). These are areas in the model where the GPS coverage is extrapolated and thus could be artifacts of smearing the signal.

[30] Two regions are evident in the seismic energy plot where the seismicity rate appears to be higher than expected from the map of calculated stressing rate. The Mammoth Lakes volcanic center shows relatively high seismic energy release in an area that is not modeled as having unusually high stressing (Figure 12). Additionally, the region around the 1992 $M = 7.3$ Landers and 1999 $M = 7.1$ Hector Mine earthquakes is of course associated with a high seismic energy release and a low stressing rate.

[31] To summarize, inconsistencies between the broad patterns of observed seismic energy release and calculated differential stressing can be explained. The exception is in the eastern San Francisco Bay region along the Calaveras, Hayward and Rodgers Creek faults where the model predicts differential stress accumulation that is not accompanied by much seismic energy release. These faults are observed to creep (Figure 1) and are allowed to in the

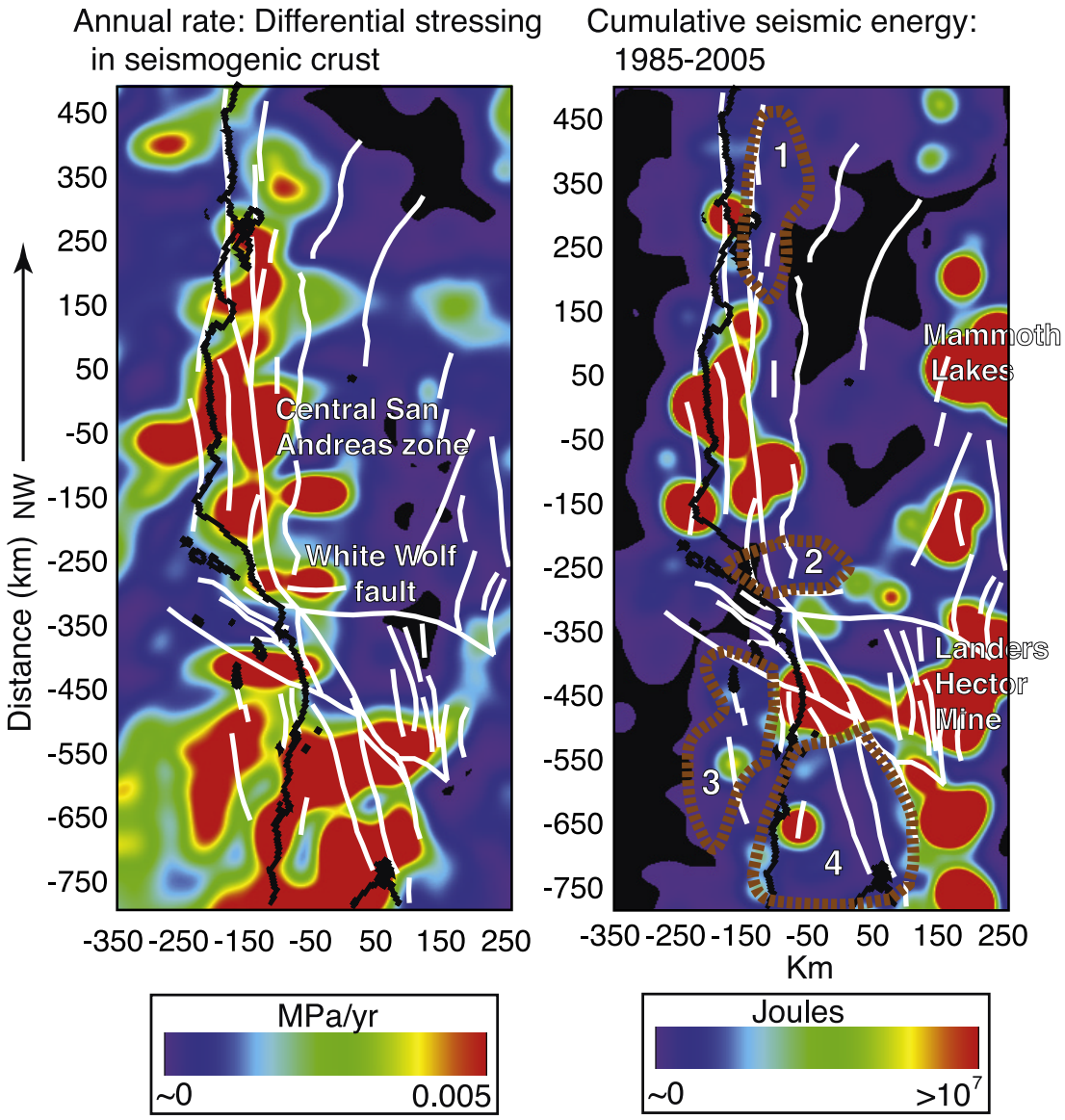

Figure 12. Comparison of differential stressing rate against calculated radiated seismic energy (events from 1985 until 2005). These plots can identify potential seismic gaps, where the modeled stressing rate is high, but seismic energy release is low (outlined with brown dashed lines). In addition, areas of high seismicity rates that are not associated with high calculated stressing rates are evident such as Mammoth Lakes volcanic center and the Landers–Hector Mine earthquake aftershock sequences.

model; stress accumulation in the model then comes from aseismic slip that does not keep pace with surface deformation and also off-fault stress that results from the creep.

3.2. Cumulative Energy Balance and Seismic Efficiency

[32] Here an attempt is made to balance energy input to the crust against seismic energy output by calculating strain

Table 1. Material Constants Used in the Three Layers of the Finite Element Model[a]

Parameter	Upper Crust Layer	Source	Lower Crust Layer	Source	Upper Mantle	Source
E Young's modulus, MPa	8×10^4	1	9×10^4	1	1.9×10^5	1
A physical constant, MPa^{-n} s^{-1}	2.0×10^{-4}	2	6.3×10^{-2}	5	5.0×10^3	6
n physical constant	1.9	2	3.1	5	3.8	6
Q_c activation energy, kJ mol^{-1}	140.6	2	276	5	492	6
ν Poisson's ratio	0.25	3	0.26	3	0.28	3
ρ density, kg m^{-3}	2.7×10^3	4	2.8×10^3	4	3.0×10^3	4

[a]Elements in the model are all viscoelastic, with rate-dependent creep behavior controlled by the temperature gradient and the listed constants. Sources: 1, *Birch* [1966]; 2, *Hansen and Carter* [1983]; 3, *Christensen* [1996]; 4, *Christensen and Mooney* [1995]; 5, *Caristan* [1982]; 6, *Carter and Tsenn* [1987].

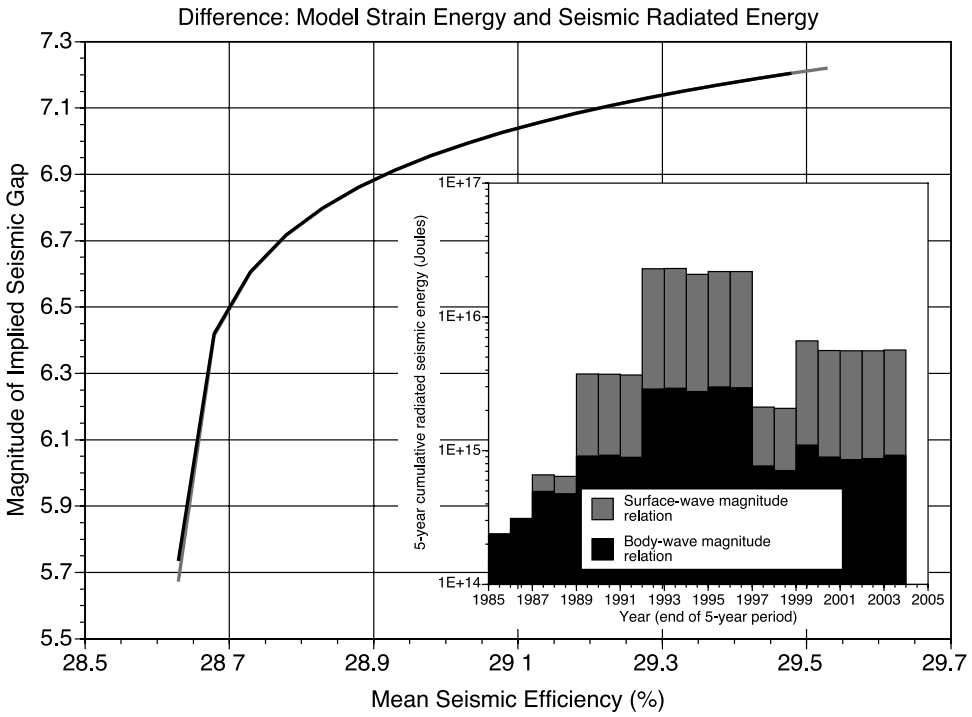

Figure 13. Balance between calculated strain energy of the whole model with the calculated radiated seismic energy. These quantities can be balanced, or there can be a growing seismic gap (vertical axis) depending on the mean seismic efficiency (horizontal axis).

energy modeled from GPS displacements and comparing that to radiated seismic energy. The cumulative strain energy can be found by integrating over the seismogenic model volume

$$\iiint W dx dy dz, \tag{7}$$

where W is the potential energy per unit volume and is given by [*Jaeger and Cook*, 1976]

$$W = \frac{1}{2}(\sigma_1\varepsilon_1 + \sigma_2\varepsilon_2 + \sigma_3\varepsilon_3), \tag{8}$$

where σ and ε are principal stress and strain magnitudes, respectively. The upper crustal layer of the finite element model is treated as the seismogenic volume, and 5 year's worth of accumulated strain energy is compared with the mean of 20 five-year calculations of radiated seismic energy calculated with equations (5) and (6) (Figure 13). Radiated seismic energy is some fraction of the total energy as $E_s = \eta E$, where η is seismic efficiency, a difficult parameter to assess because there are few reliable measurements of total energy [e.g., *Udias*, 1999]. Estimates of shallow earthquake seismic efficiency from laboratory, explosive source, and empirical observations tend to be low, ranging from about 1% to 6% [*Dobrovol'skiy*, 1994; *McGarr*, 1999; *Mori and Tanaka*, 2002]. To balance cumulative strain energy against seismic energy it was thus necessary to consider a range of seismic efficiency; in Figure 13, it is shown that small variation in this parameter allows a range from energy balance up to a cumulative seismic gap equivalent $M\sim7$ earthquake per 5-year period. Cumulative strain energy could be balanced against radiated seismic energy using a seismic efficiency value of about 28%. This relatively high value compared with observations is probably a result of averaging a large crustal volume, much of which is aseismic.

[33] I examined the modeled energetics of a smaller part of the crust by selecting elements within 10 km of either side of a 100-km-long segment of the Hayward-Rodgers Creek fault. Over a 5-year period of stress accumulation modeled from GPS displacements, this volume is calculated to have acquired $\sim 8 \times 10^{14}$ J of strain energy. The accumulated differential stress in the volume amounts to $\sim$0.64 MPa in 5 years. Mean radiated energy over 5-year periods from earthquakes occurring within ±10 km of the Hayward fault amounts to about $5 \cdot 10^{10}$ Joules, negligible in comparison to calculated strain energy. If a 28% seismic efficiency value from the cumulative balance is used, then a M = 6.7 earthquake would be expected every 5 years, clearly a much higher rate than observed (one per $\sim$150–250 years [*WGCEP*, 2003]). To balance calculated strain energy along the Hayward fault against the expected rate of M = 6.7 events, the seismic efficiency must only be about 0.8% to 1.3%, more in accord with the observed 1% to 6% [*Dobrovol'skiy*, 1994; *McGarr*, 1999; *Mori and Tanaka*, 2002]. The large difference between seismic efficiency (28% versus 1%) necessary to balance cumulative energy and local energy may result from most model strain occurring near the San Andreas plate boundary fault system, of which the Hayward fault is a part. Alternatively, if Hayward-Rodgers Creek fault seismic

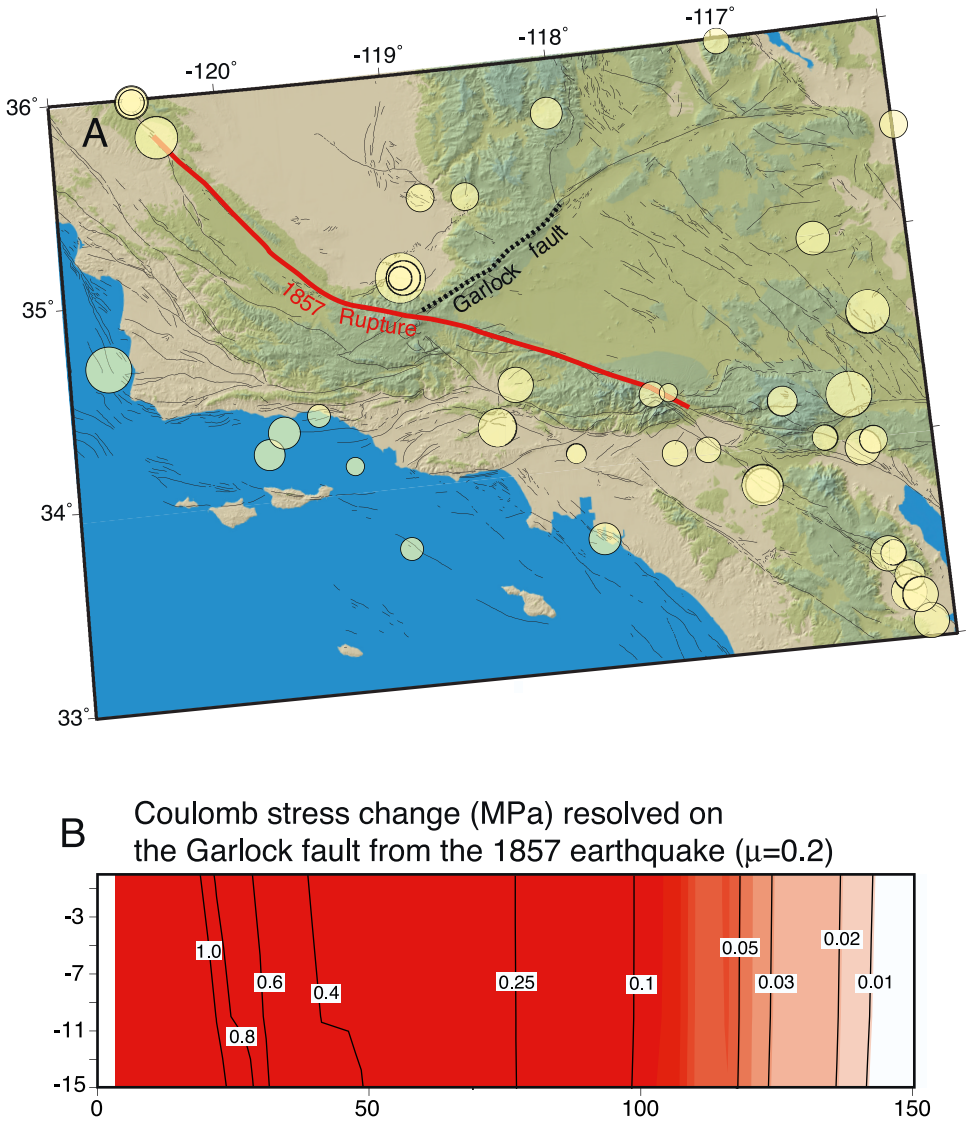

Figure 14. (a) Location of the 1857 earthquake rupture used to calculate the static stress increase on (b) the left-lateral Garlock fault. Locations of $M \geq 5.5$ earthquakes since 1857 are also shown as yellow circles.

efficiency exceeds ~1%, then there is likely a growing seismic gap.

3.3. Stressing Rate on Specific Faults

[34] In this section, a case study is presented to illustrate how modeled tectonic stressing rates might be useful in understanding fault interactions in California. The 1857 $M \sim 7.8$ [*Ellsworth*, 1990] Fort Tejon earthquake ruptured about 300 km of the San Andreas fault in southern California (Figure 14). *Harris and Simpson* [1996] found that calculated static stress changes from the 1857 earthquake were consistent with nearly every $M \geq 5.5$ southern California earthquake between 1857 and 1907. In this section I investigate the curious behavior of the Garlock fault (Figure 14 for location) after the 1857 earthquake.

[35] What is odd about post-1857 Garlock fault activity is that there has been so little; there have been no $M \geq 5.5$ earthquakes on it since 1857 despite quite large computed static stress increases from the Fort Tejon earthquake (Figure 14). Calculated Coulomb stress increase on the west end of the Garlock fault exceeds 1 MPa regardless of friction coefficient. Other faults with computed post-1857 static stress increases showed relatively high levels of $M \geq 5.5$ events [*Harris and Simpson*, 1996]. However, if this process is examined in the context of the modeled tectonic stressing results resolved onto the Garlock fault, it may be consistent with the stress transfer model.

[36] A Coulomb stressing rate on the Garlock fault was computed from the time series of the calculated stress tensor using the methods described in Appendix A. Calculations show that current crustal deformation acts to clamp the Garlock fault, which causes a net negative secular Coulomb stressing rate on the fault (Figure 15). Thus while slip on the San Andreas fault tends to increase

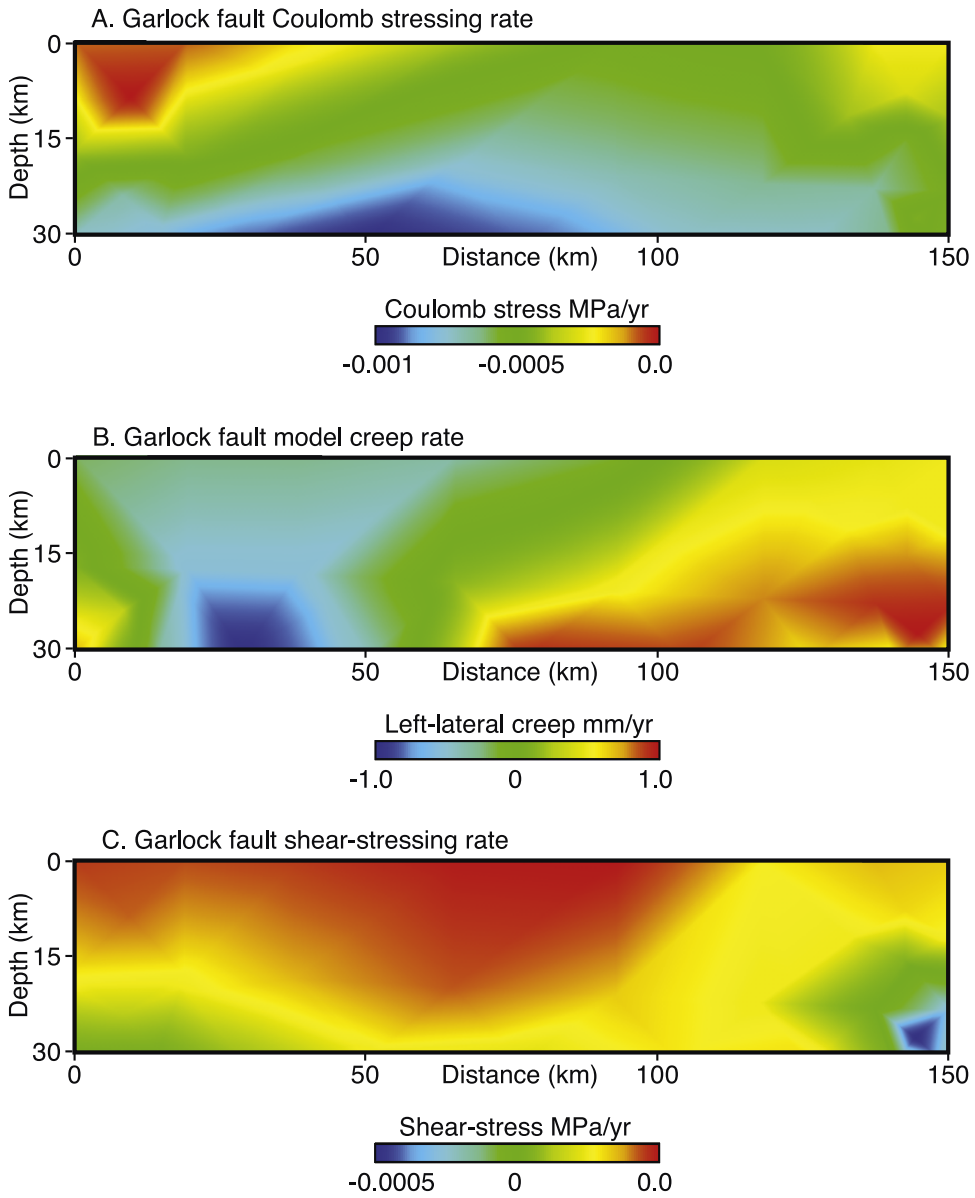

Figure 15. (a) Coulomb stressing rate on the Garlock fault (segment location shown in Figure 14a); the entire segment is calculated to have a net negative stressing rate. (b) Modeled Garlock fault creep rate, which correlates with (c) the calculated shear stressing rate.

Coulomb stress on the Garlock fault, interseismic strain tends to reduce it. This is of course only true if recently observed GPS observations characterize strain throughout the San Andreas fault seismic cycle. If so, then the state of stress could have been very low on the Garlock fault in 1857, making earthquake triggering unlikely. The tectonic stressing rate is about -5×10^{-3} MPa yr^{-1} in the center of the modeled segment of the Garlock fault, implying that it would take about 200 to 800 years to erase the 1857 static stress increase (0.1–0.4 MPa). Stress could thus gradually accumulate on the Garlock fault depending on the recurrence interval of 1857-like earthquakes on the San Andreas fault. This complicated loading pattern is consistent with the irregular pattern of earthquake recurrence observed on the Garlock fault (individual event spacing ranges from 190 to 1545 years [*McGill and Rockwell*, 1998]).

4. Conclusions

[37] GPS-derived displacements were used to distort a finite element model of California and surroundings. Mapping the resulting differential stress in the crust revealed a broad, ~200-km-wide zone of highest stressing rate that corresponds with the San Andreas and related faults. For the most part, this zone correlates with the majority of seismic activity and calculated radiated energy release. A potential "gap" where stressing rates are relatively high compared with seismic energy was noted in the eastern San Francisco Bay region along the Hayward and Rodgers Creek fault,

although it is unclear what role aseismic slip may play on these creeping faults. The California finite element model was built with topography and variable crustal thickness; away from the plate boundary, I note areas where crustal motions are consistent with aseismic topographic collapse. Balancing input strain energy against radiated seismic energy can be achieved for the whole model using a ~28% seismic efficiency value; balancing an individual plate boundary fault where a seismic gap was postulated (the Hayward-Rodgers Creek system), required a much smaller (~1%) efficiency.

[38] Model-derived stressing rate values were used for a study of stress interaction between the 1857 M~7.8 Ft. Tejon earthquake and the Garlock fault. An apparent paradox of very high static stress transfer that resulted in no $M > 5$ earthquakes can be resolved because calculated Coulomb stressing rates on the Garlock fault are very low to negative. I thus suggest that the Garlock fault is stressed only by slip on the San Andreas fault, and that it does not get loaded by secular motions.

Appendix A: Calculation of Fault-Stressing Rates From Stress Tensor Components

[39] The rate of Coulomb stressing (equation (1)) on defined fault planes can be calculated if the stress tensor components have been defined over time with the finite element model [e.g., *Jaeger and Cook*, 1976]. The normal stress (σ_n) is

$$\sigma_n = l_1 p_x + m_1 p_y + n_1 p_z, \tag{A1}$$

where

$$\begin{aligned} p_x &= l_1\sigma_x + m_1\tau_{xy} + n_1\tau_{zx} \\ p_y &= l_1\tau_{xy} + m_1\sigma_y + n_1\tau_{zy} \\ p_z &= l_1\tau_{xz} + m_1\tau_{yz} + n_1\sigma_z \end{aligned} \tag{A2}$$

with l_1, m_2, and n_3 being direction cosines between the model coordinate axes and the axes defining a plane on the fault surface. Similarly, shear stresses on the fault plane ($\tau_{x'y'}$) can be found from

$$\tau_{x'y'} = l_2 q_x + m_2 q_{xy} + n_2 q_{xz}, \tag{A3}$$

where

$$\begin{aligned} q_x &= l_1\sigma_x + m_1\tau_{yx} + n_1\tau_{zx} \\ q_{xy} &= l_1\tau_{xy} + m_1\sigma_y + n_1\tau_{zy} \\ q_{xz} &= l_1\tau_{xz} + m_1\tau_{yz} + n_1\sigma_z. \end{aligned} \tag{A4}$$

These relations can be used to resolve shear stress in the fault rake direction. Coulomb stressing rates then can be determined from the changes in the shear and normal stress components over time. The fault can be divided up into many small patches such that stressing rates may be computed on surfaces of any complexity and can be found for varying rake angles.

[40] **Acknowledgments.** I thank Associate Editor Steven Cohen and two anonymous reviewers for helpful and perceptive comments. Beth Erlund helped me pull together data on crustal structure, heat flow, and GPS velocities used in the modeling.

References

Anderson, E. M. (1951), *The Dynamics of Faulting and Dyke Formation*, 206 pp., Oliver and Boyd, White Plains, N. Y.

Argus, D. F., and R. G. Gordon (2001), Present tectonic motion across the Coast Ranges and San Andreas fault system in central California, *Geol. Soc. Am. Bull.*, *113*, 1580–1592.

Beaudoin, B. C., J. A. Hole, S. L. Klemperer, and A. M. Trehu (1998), Location of the southern edge of the Gorda slab and evidence for an adjacent asthenospheric window: Results from seismic profiling and gravity, *J. Geophys. Res.*, *103*, 30,101–30,115.

Birch, F. (1966), Compressibility; elastic constants, *Mem. Geol. Soc. Am.*, *97*, 97–173.

Caristan, Y. (1982), The transition from high temperature creep to fracture in Maryland diabase, *J. Geophys. Res.*, *87*, 6781–6790.

Carter, N. L., and M. C. Tsenn (1987), Flow properties of the lithosphere, *Tectonophysics*, *136*, 27–63.

Catchings, R. D., and W. M. Kohler (1996), Reflected seismic waves and their effect on strong shaking during the 1989 Loma Prieta, California earthquake, *Bull. Seismol. Soc. Am.*, *86*, 1401–1416.

Colburn, R. H., and W. D. Mooney (1986), Two-dimensional velocity structure along the synclinal axis of the great valley, California, *Bull. Seismol. Soc. Am.*, *76*, 1305–1322.

Christensen, N. I. (1996), Poisson's ration and crustal seismology, *J. Geophys. Res.*, *101*, 3139–3156.

Christensen, N. I., and W. D. Mooney (1995), Seismic velocity structure and composition of the continental crust: A global view, *J. Geophys. Res.*, *81*, 3047–3054.

d'Alessio, M. A., I. A. Johanson, R. Bürgmann, D. A. Schmidt, and M. H. Murray (2005), Slicing up the San Francisco Bay Area: Block kinematics and fault slip rates from GPS-derived surface velocities, *J. Geophys. Res.*, *110*, B06403, doi:10.1029/2004JB003496.

DeMets, C., R. G. Gordon, D. F. Argus, and S. Stein (1994), Effect of recent revisions to the geomagnetic reversal time scale on estimates of current plate motions, *Geophys. Res. Lett.*, *21*, 2191–2194.

Dixon, T. H., M. Miller, F. Farina, H. Wang, and D. Johnson (2000), Present-day motion of the Sierra Nevada block and some tectonic implications for the Basin and Range province, North American Cordillera, *Tectonics*, *19*, 1–24.

Dobrovol'skiy, I. P. (1994), Seismic efficiency of the tectonic earthquake, *Phys. Solid Earth, Engl. Transl.*, *30*, 462–465.

Ellsworth, W. L. (1990), Earthquake history, in *The San Andreas Fault System, California*, edited by R. E. Wallace, *U.S. Geol. Surv. Prof. Pap.*, *1515*, 153–181.

Fliedner, M. M., and S. Ruppert (1996), Three-dimensional crustal structure of the southern Sierra Nevada from seismic fan profiles and gravity modeling, *Geology*, *24*, 367–370.

Freed, A. M., and R. Bürgmann (2004), Evidence of powerlaw flow in the Mojave desert mantle, *Nature*, *430*, doi:10.1038/nature02784, 548–551.

Fuis, G. S., T. Ryberg, N. J. Godfrey, D. A. Okaya, and J. M. Murphy (2001), Crustal Structure and tectonics from the Los Angeles Basin to the Mojave Desert, southern California, *Geology*, *29*, 15–18.

Godfrey, N. J., B. C. Beaudoin, and S. L. Klemperer (1997), Ophiolitic basement to the Great Valley forearc basin, California, from seismic and gravity data: Implications for crustal growth at the North American continental margin, *Geol. Soc. Am. Bull.*, *108*, 1536–1562.

Gutenberg, B., and C. F. Richter (1942), Earthquake magnitude, intensity, energy, and acceleration, *Bull. Seismol. Soc. Am.*, *32*, 163–191.

Gutenberg, B., and C. F. Richter (1956), Magnitude and energy of earthquakes, *Ann. Geofis.*, *9*, 1–15.

Hammond, W. C., and W. Thatcher (2004), Contemporary tectonic deformation of the Basin and Range province, western United States: 10 years of observation with the Global Positioning System, *J. Geophys. Res.*, *109*, B08403, doi:10.1029/2003JB002746.

Hansen, F. D., and N. L. Carter (1983), Semibrittle creep of dry and wet Westerly granite at 1000 MPa, *Proc. U.S. Symp. Rock Mech., 24th*, 429–447.

Harris, R. A., and R. W. Simpson (1996), In the shadow of 1857: The effect of the great Ft. Tejon earthquake on subsequent earthquakes in southern California, *Geophys. Res. Lett.*, *23*, 229–232.

Hauksson, E. (2000), Crustal structure and seismicity distribution adjacent to the pacific and North America plate boundary in southern California, *J. Geophys. Res.*, *105*, 13,875–13,903.

Hauksson, E., and J. S. Haase (1997), Three-dimensional V_p and V_p/V_s velocity models of the Los Angeles basin and central Transverse Ranges, California, *J. Geophys. Res.*, *102*, 5423–5453.

Henstock, T., J. A. Levander, and J. A. Hole (1997), Deformation in the lower crust of the San Andreas Fault System in northern California, *Science*, *278*, 2.

Holbrook, W. S., and W. D. Mooney (1987), The crustal structure of the axis of the Great Valley California, *Tectonophysics*, *140*, 49–63.

Holbrook, W. S., T. M. Brocher, U. S. ten Brink, and J. A. Hole (1996), Crustal Structure of a transform plate boundary: San Francisco Bay and the central California continental margin, *J. Geophys. Res.*, *101*, 22,311–22,334.

Howie, J. M., K. C. Miller, and W. U. Savage (1993), Integrated crustal structure across the south central California Margin: Santa Lucia escarpment to the San Andreas Fault, *J. Geophys. Res.*, *98*, 8173–8196.

Jaeger, J. C., and N. G. W. Cook (1976), *Fundamentals of Rock Mechanics*, 585 pp., John Wiley, Hoboken, N. J.

Kirby, S. H., and A. K. Kronenberg (1987), Rheology of the lithosphere: Selected topics, *Rev. Geophys.*, *25*, 1219–1244.

Lachenbruch, A. H. (1968), Preliminary geothermal model of the Sierra Nevada, *J. Geophys. Res.*, *73*, 6977–6989.

Leitner, B., A. M. Trehu, and N. J. Godfrey (1998), Crustal structure of the northwestern Vizcaino block and Gorda Escarpment, offshore northern California, and implications for postsubduction deformation of a paleoaccretionary margin, *J. Geophys. Res.*, *103*, 23,795–23,812.

Lisowski, M., J. C. Savage, and W. H. Prescott (1991), The velocity field along the San Andreas fault in central and southern California, *J. Geophys. Res.*, *96*, 8369–8389.

Lonsdale, P. (1989), Geology and tectonic history of the Gulf of California, in *The Geology of North America,* vol. N, *The Eastern Pacific Ocean and Hawaii*, edited by E. L. Winterer, D. M. Hussong, and R. W. Decker, pp. 499–521, Geol. Soc. of Am., Boulder, Colo.

Manaker, D. M., A. J. Michael, and R. Bürgmann (2005), Subsurface structure and kinematics of the Calaveras–Hayward Fault stepover from three-dimensional V_p and seismicity, San Francisco Bay region, California, *Bull. Seismol. Soc. Am.*, *95*, 446–470, doi:10.1785/0120020202.

McGarr, A. (1999), On relating apparent stress to the stress causing earthquake fault slip, *J. Geophys. Res.*, *104*, 3003–3011.

McGill, S., and T. Rockwell (1998), Ages of Holocene earthquakes on the central Garlock fault near El Paso Peaks, *California, J. Geophys. Res.*, *103*, 7265–7279.

Meissner, R. (1986), *The Continental Crust*, *Int. Geophys. Ser.*, vol. 34, 426 pp., Elsevier, New York.

Melbourne, T., and D. Helmberger (2001), Mantle control of plate boundary deformation, *Geophys. Res. Lett.*, *28*, 4003–4006.

Mori, J., and H. Tanaka (2002), Energy budget of the 1999 Chichi, Taiwan earthquake, *Eos Trans. American Geophysical Union*, *83*(47), Fall Meet. Suppl., Abstract S71E-09.

Page, B. M., and T. M. Brocher (1993), Thrusting of the central California margin over the edge of the Pacific plate during the transform regime, *Geology*, *21*, 635–638.

Parsons, T. (2002), Post-1906 stress recovery of the San Andreas fault system calculated from three-dimensional finite element analysis, *J. Geophys. Res.*, *107*(B8), 2162, doi:10.1029/2001JB001051.

Parsons, T., and J. McCarthy (1996), Crustal and upper mantle velocity structure of the Salton Trough, southeast California, *Tectonics*, *15*, 456–471.

Prodehl, C. (1979), Crustal structure of the western United States, *U.S. Geol. Surv. Prof. Pap.*, *1034*, 74 pp.

Savage, J. C., J. L. Svarc, and W. H. Prescott (1999), Geodetic estimates of fault slip rates in the San Francisco Bay area, *J. Geophys. Res.*, *104*, 4995–5002.

Savage, J. C., W. Gan, W. H. Prescott, and J. L. Svarc (2004), Strain accumulation across the Coast Ranges at the latitude of San Francisco, 1994–2000, *J. Geophys. Res.*, *109*, B03413, doi:10.1029/2003JB002612.

Schmidt, D. A., R. Bürgmann, R. M. Nadeau, and M. d'Alessio (2005), Distribution of aseismic slip rate on the Hayward fault inferred from seismic and geodetic data, *J. Geophys. Res.*, *110*, B08406, doi:10.1029/2004JB003397.

Segall, P., and J. L. Davis (1997), GPS applications for geodynamics and earthquake studies, *Annu. Rev. Earth Planet. Sci.*, *25*, 301–336.

Smith, B., and D. Sandwell (2003), Coulomb stress accumulation along the San Andreas Fault system, *J. Geophys. Res.*, *108*(B6), 2296, doi:10.1029/2002JB002136.

Stein, R. S., G. C. P. King, and J. Lin (1992), Change in failure stress on the southern San Andreas fault system caused by the 1992 magnitude = 7.4 Landers earthquake, *Science*, *258*, 1328–1332.

ten Brink, U. S., J. Zhang, T. M. Brocher, D. A. Okaya, K. D. Klitgord, and G. S. Fuis (2000), Geophysical evidence for the evolution of the California Inner Continental Borderland as a metamorphic core complex, *J. Geophys. Res.*, *105*, 5835–5857.

Thatcher, W. (1990), Present-day crustal movements and the mechanics of cyclical deformation, *U.S. Geol. Surv. Prof. Pap.*, *1515*, 283 pp.

Udias, A. (1999), *Principles of Seismology*, 475 pp., Cambridge Univ. Press, New York.

Walter, A. W., and W. D. Mooney (1982), Crustal structure of the Diablo and Gabilan ranges, central California: A reinterpretation of existing data, *Bull. Seismol. Soc. Am.*, *72*, 1567–1590.

Wells, R. E., C. S. Weaver, and R. J. Blakely (1998), Fore-arc migration in Cascadia and its neotectonic significance, *Geology*, *26*, 759–762.

Working Group on California Earthquake Probabilities (WGCEP) (2003), Earthquake probabilities in the San Francisco Bay region: 2002 to 2031, *U.S. Geol. Surv. Open File Rep., 03-214*.

T. Parsons, U.S. Geological Survey, 345 Middlefield Road, MS 999, Menlo Park, CA 94025, USA. (tparsons@usgs.gov)